

Time stability of the dynamic behaviour of a 3D-printed airless wheel by stereolithography

Alessandro Annessi¹, Antonino Quattrocchi², Simone Pasinetti³, Milena Martarelli⁴, Paolo Chiariotti⁵, Paolo Castellini⁴, Gianluca Rossi⁶, Roberto Montanini²

¹ Department of Agricultural, Food and Environmental Sciences, Università Politecnica delle Marche, Ancona, Italy

² University of Messina, Department of Engineering, Messina Italy

³ Department of Mechanical and Industrial Engineering, University of Brescia, Brescia, Italy

⁴ Department of Industrial Engineering and Mathematical Sciences, Università Politecnica delle Marche, Ancona, Italy

⁵ Department of Mechanical Engineering, Politecnico di Milano, Milan, Italy

⁶ Department of Engineering, University of Perugia, Perugia, Italy

ABSTRACT

In this paper, the dynamic behavior of an airless wheel made by additive manufacturing is investigated. A lattice geometry is chosen as the cyclic pattern from which the wheel is built. Initially, a linear numerical model is used to preliminarily assess resonance frequency and mode shapes of the wheel. Afterwards, specimens were tested twice, in August 2020 and after six months, highlighting a relevant frequency and damping shift in the vibrational response. To better understand the reason behind the change over time in the wheel dynamic behavior, dedicated structural dynamics tests at varying temperature and humidity set points were performed in an environmental chamber, consisting in measuring the wheel vibrational response when subjected to temperature and humidity variation.

Section: RESEARCH PAPER

Keywords: Lattice structures; additive manufacturing; finite element modelling; applied mathematics; modal analysis; dynamic characterization

Citation: Alessandro Annessi, Antonino Quattrocchi, Simone Pasinetti, Milena Martarelli, Paolo Chiariotti, Paolo Castellini, Gianluca Rossi, Roberto Montanini, Time stability of the dynamic behaviour of a 3D-printed airless wheel by stereolithography, Acta IMEKO, vol. 12, no. 4, article 45, December 2023, identifier: IMEKO-ACTA-12 (2023)-04-45

Section Editor: Laura Fabbiano, Politecnico di Bari, Italy

Received October 13, 2023; **In final form** December 11, 2023; **Published** December 2023

Copyright: This is an open-access article distributed under the terms of the Creative Commons Attribution 3.0 License, which permits unrestricted use, distribution, and reproduction in any medium, provided the original author and source are credited.

Funding: This work was supported by the Ministry of Education, University and Research in Italy (MIUR) under the Research Project of National Interest (PRIN2015) "Experimental techniques for the characterization of the effective performances of trabecular morphology structures realized in additive manufacturing".

Corresponding author: Alessandro Annessi, e-mail: a.annessi@univpm.it

1. INTRODUCTION

Additive Manufacturing (AM) is defined by the *American Society for Testing and Materials* (ASTM) as "a process of joining materials to make objects from 3D model data, usually layer upon layer, as opposed to subtractive manufacturing methodologies" [1]. Nowadays, AM technology addresses both academia and industry, given its advantages in delivering customized components for a wide variety of applications. In the aerospace field, additive manufacturing is widely exploited for high-profile applications, reducing component weight, enhancing design complexity and thermal performances [2]-[5]. Furthermore, 3D printing could be also used for manufacturing electronic circuits, stretchable sensors and antennas [6], [7]. In the biomedical field, anatomical models, customized implants and organs could be

printed using standard, medical grade materials and biomaterials [8]-[11]. The strength of AM is the ability to create customized complex geometries in a reasonable time and at relatively low cost (in case of low production volumes). Technology downsides are related to the limited variety of available materials, material mechanical properties inhomogeneity, and surface quality [12]-[17]. This led to the need of evaluating the uncertainty of the manufactured specimen in terms of geometry and mechanical properties [18]-[20].

AM is usually associated with the realization of complex structures such as lattice, periodic, chiral, or topology-optimized structures, which could not be made by exploiting traditional manufacturing techniques. Such complex structures are increasingly used in modern designs for their peculiar mechanical properties relating mechanical performances over low densities,

shock absorbing, acoustic and vibration isolation, compliance [21]-[23].

The field of application of AM considered in this paper is the production process of an airless wheel, i.e., an unconventional wheel that does not rely on air pressure to support weight and absorb shock due to irregular terrain. Airless wheels are mainly used on difficult terrain to increase wheel traction and avoid wheel failure, typically on rovers employed in planetary exploration missions [24]. Lately, AM technique has been assessed to be useful for the development and realization of spoke complex shapes for airless wheels [25].

In our application, Stereolithography (SLA) technique is used to realize an airless wheel prototype. SLA is defined by ASTM as "a vat photopolymerization process used to produce parts from photopolymer materials in a liquid state using one or more lasers to selectively cure to a predetermined thickness and harden the material into shape layer upon layer" [1]. This technique is widely exploited in high-precision application, given its capability to achieve in plane resolutions on the order of tens of μm (depending on laser spot, resin type and curing process).

As in all 3D printing processes, material properties of the final part depend on the manufacturing technique used. In the case of SLA, working parameters such as laser power, layer thickness and post-curing affect the mechanical properties of the final product [26]. In particular, the UV curing process ensures the needed stiffness of the component when removed from the printer. If using plastics as printing material, another uncertainty related to environmental ageing of the material needs to be taken into account. In fact, environmental ageing can cause material stiffening and brittleness [27]-[32].

AM mechanical material properties dependency on temperature and humidity have been widely explored in static conditions whilst their dependency on dynamic conditions is still under investigation [33].

On a previous work [34], the authors have focused on the applicability of non-contact techniques, such as Digital Image Correlation (DIC) and Thermoelastic Stress Analysis (TSA) to evaluate strain and stress fields on airless wheels produced by 3D printing. This paper aims at discussing how the dynamic behaviour of components produced by AM, in particular considering the same 3D printed airless wheels investigated in [34], is affected by material ageing. The document is organized as follows. In Section 2, the airless wheel cyclic design is presented with printing details relative to the process and the material chosen. A finite element model, targeted to retrieve the numerical eigenfrequencies and mode shapes of the structure, is also presented. Section 3 reports the results of the Experimental Modal Analysis (EMA) carried out on the two specimens manufactured. Measurements were performed twice, in August 2020 and after six months. Sections 4 reports the dynamic characterization of the two specimens during performed during tests carried out in an environmental chamber. Finally, conclusions are drawn and reported in Section 0.

2. AIRLESS WHEEL

2.1. Design prototype

The airless wheel design presented in this work consists of the cyclic repetition of a lattice pattern inspired by the non-pneumatic tire proposed by Manesh et al. from the Resilient Technologies LLC, University of Wisconsin- Madison [35]. The geometry is designed following a regular pattern of fixed angular amplitude (36°), extruded in the axial direction of the same

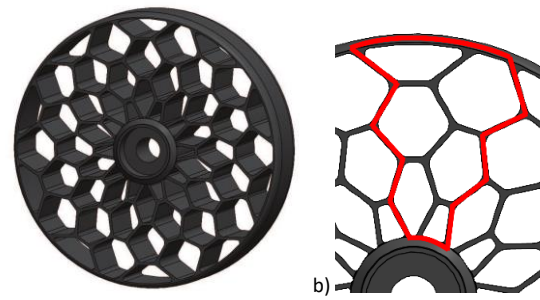


Figure 1. Airless wheel lattice design: a) Airless wheel, b) Periodic lattice pattern.

Table 1. 3D printing parameters used for the airless wheel prototypes.

AM technique	SLA
Material	Black V4
Dimension of support points in mm	0.6
Layer thickness in μm	50
Printing time in h	9.15
Number of layers	1003
Material volume or weight	72 ml
Orientation in $^\circ$	15

wheel. The lattice structure is obtained by connecting the intersection points of four circular crowns of equal width along the diameter and ten circular sectors of the wheel through a "zig-zag" criterion. The thickness of each trabecula is always kept the same. The final geometry is depicted in Figure 1a whilst the characteristic cyclic pattern is highlighted in Figure 1b in red. The whole wheel, drawn repeating the cyclic pattern for 10 times, is obtained as is shown in Figure 1a. It has a diameter of 100 mm and a width of 22 mm.

The component is produced by AM technology, specifically Stereolithography (SLA). In our case, Form 2 by Formlabs is the 3D printer used with a standard resin. The Form 2 declared in-plane resolution is $25\ \mu\text{m}$ while its out-of-plane resolution is about $20\ \mu\text{m}$. The printing process parameters are listed in Table 1. Two airless wheels, from here on addressed as W1 and W2, were printed using the same printing settings and the same photopolymeric resin (Formlabs Black V4). Material properties, collected from the manufacturer datasheet, are reported in Table 2. The orientation angle of the plane on which the wheel lies during the printing process was of 15° for both wheels. Both samples have been post-cured with UV light (wavelength of 405 nm) at 60°C for 30 minutes in climatic chamber, flipping each side every 15 minutes, to complete the solidification process and enhance the mechanical properties of the structure. The raw component along with printing supports after the wash in isopropyl alcohol is shown in Figure 2a whilst a front view of the final cleaned prototype is depicted in Figure 2b.

Table 2. Mechanical properties of the FormLabs Black standard resin.

Formlabs Black V4 standard resin properties	
Density in g/cm^3	1.15
Tensile Modulus in GPa	2.8
Flexural Modulus in GPa	2.2
Ultimate Tensile Strength in MPa	65
Elongation at failure in %	6.2
Longitudinal wave speed in m/s	1560.4
Shear wave speed in m/s	1383.1

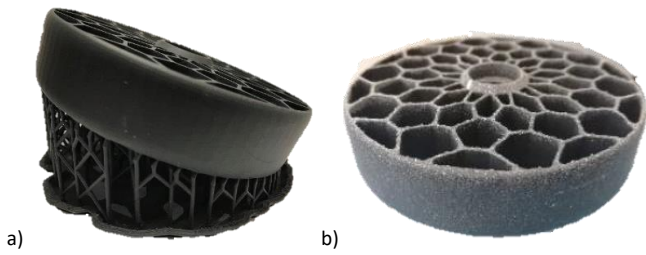


Figure 2. Airless wheel prototype manufactured by SLS process: a) Raw component with printing supports, b) Front view of the prototype.

2.2. Finite element model

A finite element model of the airless wheel in free-free condition is computed by means of COMSOL Multiphysics® using the solid mechanics module to retrieve the eigenfrequencies of the system and the related mode shapes.

The material is considered as linear elastic for the analysis. The material properties specified by the supplier were used in the simulation. The mesh used for the discretization of the component is shown in Figure 3. It consists of tetrahedral elements characterized by an average element quality of 66 % and a maximum element size of 9.26 mm. The minimum element size is a trade-off between the need to discretize the complex geometry accurately and have a reasonable number of degrees of freedom. The maximum frequency to be investigated would be around 5 kHz, leading a theoretical maximum element size for the mesh equal to $\lambda_{max} = (c_{shear}/f_{max})/5 = 55.32$ mm, considering 5 elements per wavelength, which is greater than the maximum element size used for the analysis.

The eigenfrequencies are indicated in Table 3 while their corresponding mode shapes are shown in Figure 4. It is worth noting that, due to the cyclic periodicity of the regular pattern of fixed angular amplitude (36 °) characterizing the structure, each mode shape has a twin mode spatially shifted around the z-axis, passing through the wheel centre.

3. DYNAMIC TEST

3.1. Modal Testing setup

EMA tests were carried out in impact testing mode over a grid of 30 measurement points equally spaced on a circumference located on the mid plane of each wheel. Three points were considered for each cyclic pattern, from which the wheel is made up. They are represented as solid circles in Figure 5, the driving point is highlighted in red. An impact hammer (PCB Piezotronics Model. 086E80 - force cell sensitivity: 19.50 mV/N) and a miniaturized accelerometer (PCB Piezotronics Model. 352C23)

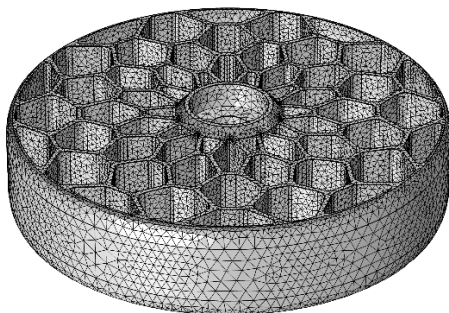


Figure 3. Mesh grid for finite element analysis.

Table 3. Numerical natural frequencies.

N. mode	Eigenfrequency in Hz
1	1643.5
2	1877.7
3	2249.5
4	2566.7
5	3094.3
6	3574.6
7	3982.4

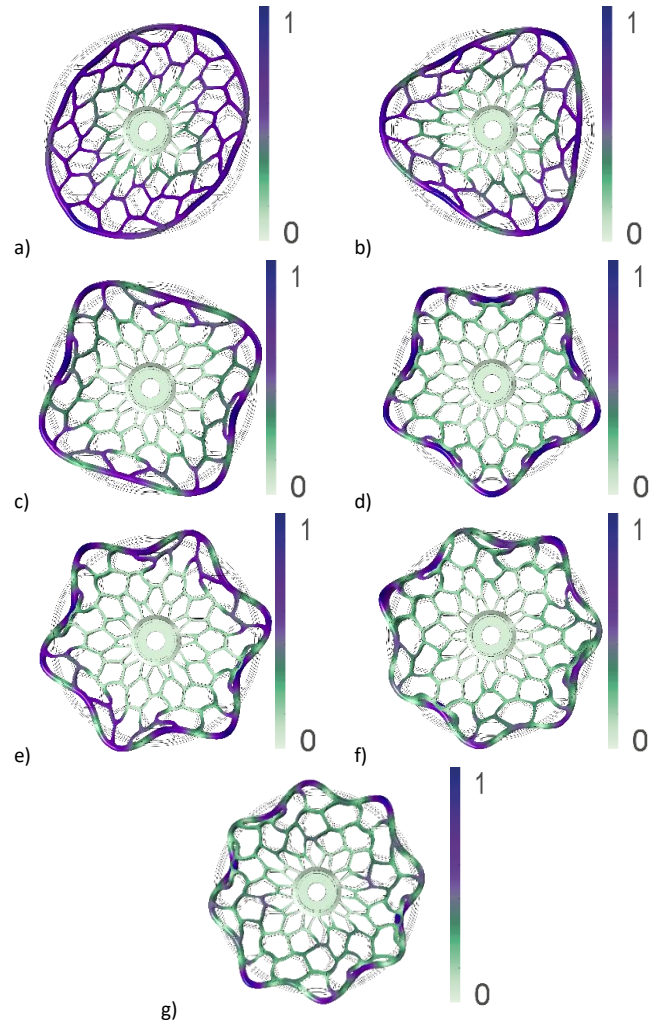


Figure 4. Numerical mode shapes: a) Mode 1, b) Mode 2, c) Mode 3, d) Mode 4, e) Mode 5, f) Mode 6, g) Mode 7.

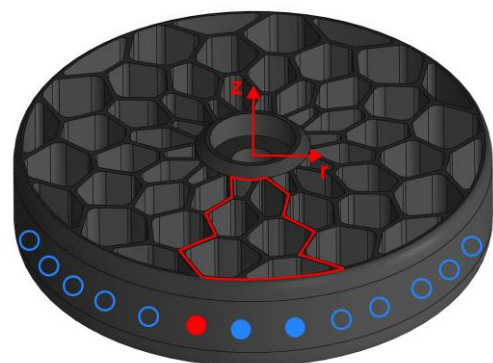


Figure 5. Frequency response function measurement grid.

Table 4. Acquisition parameters for Frequency Response Function measurements.

Acquisition parameters	
Bandwidth in Hz	5120
Spectral lines	4097
Acquisition time in s	0.8
Frequency resolution in Hz	1.25
N. of averages for each measurement point	5

with a sensitivity of 5.39 mV/g were used in the analysis. Both excitation and measurement directions are radial with respect to the polar reference frame located in the centre of the wheel. The frequency Response Functions (FRFs) characterizing each measurement point were obtained according to the roving accelerometer approach. The acquisition parameters for the measurements are reported in Table 4.

The airless wheel was placed above a foam rubber sheet to emulate a free constraint. The modal parameters were extracted exploiting the PolyMAX Plus algorithm available in the Simcenter Testlab package.

3.2. Results

The driving point FRFs for the two wheels tested are shown in Figure 6. Experimental measurements on both wheels were performed twice, i.e. in August 2020 and then, after six months, in March 2021. The eigenfrequencies obtained from EMA for both measurement campaigns are shown respectively in Table 5 and Table 6. Their relative mode shapes are depicted in Figure 7. The results obtained with the numerical linear model are in good agreement with those retrieved from the experimental tests in terms of mode shape order and resonance frequency. To prove this statement, the relative error in percentage (PE) between the experimental and the numerical resonance frequencies for both tests carried out in August 2020 and March 2021 is reported in Table 7. The percentage error – given in % – is calculated as:

$$PE(i) = \frac{f_n^{exp}(i) - f_n^{num}(i)}{f_n^{exp}(i)} \cdot 100 \quad (1)$$

with $i = 1:n$, where n is the number of resonance frequencies. The experimental results obtained in August 2020 are characterized by the lower error (with a maximum value of 5.4 % for W1 and 6.2 % for W2) and are, in fact, closer to the production date of the component. On the contrary, results obtained in March 2021 are characterized by a greater error, with a maximum value of 16.5 % for W1 and 14.1 % for W2, which

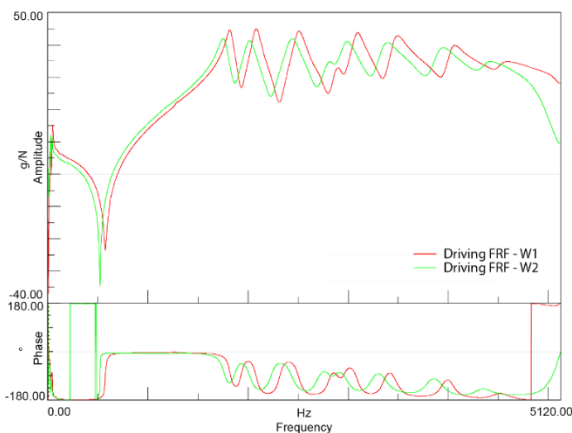


Figure 6. Driving point frequency response function.

Table 5. Natural frequencies for the August 2020 measurement campaign.

W1		W2	
f_n in Hz	η in %	f_n in Hz	η in %
1601.3	3.61	1570.5	3.75
1818.0	3.62	1768.1	3.63
2195.0	3.56	2128.5	3.64
2713.4	3.25	2657.1	3.56
3061.3	3.47	3004.5	3.37
3544.7	3.05	3477.0	3.42
3919.3	3.55	3888.5	3.76

Table 6. Natural frequencies for the March 2021 measurement campaign.

W1		W2	
f_n in Hz	η in %	f_n in Hz	η in %
1818.0	1.70	1771.4	2.18
2074.5	1.55	2022.5	2.18
2500.3	1.74	2433.3	2.29
3072.7	1.70	2986.7	2.11
3491.6	1.63	3375.0	2.22
4077.8	1.68	3925.0	2.24
4440.1	1.99	4381.6	2.25

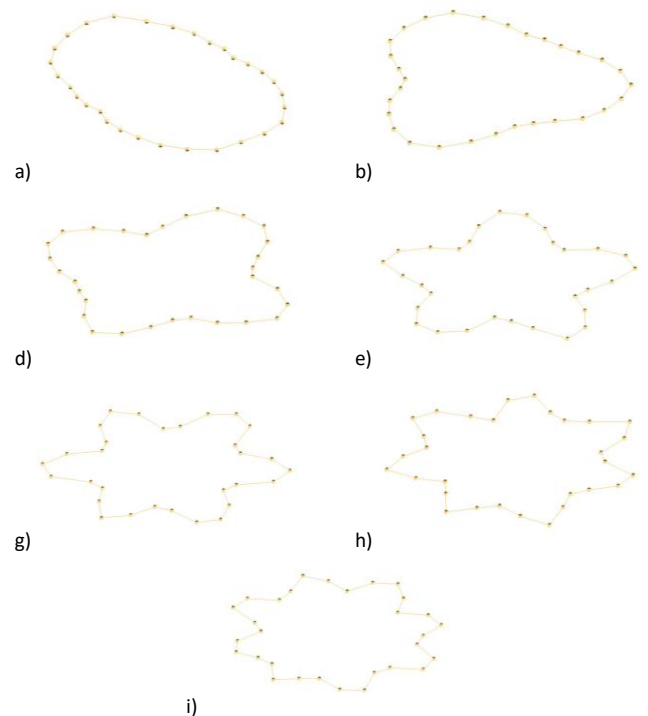


Figure 7. Experimental mode shapes: a) Mode 1, b) Mode 2, d) Mode 3, e) Mode 4, g) Mode 5, h) Mode 6, i) Mode 7.

Table 7. Relative error between numerical and experimental resonance frequency.

August 2020		March 2021	
W1	W2	W1	W2
-2.6 %	-4.6 %	9.6 %	7.2 %
-3.3 %	-6.2 %	9.5 %	7.2 %
-2.5 %	-5.7 %	10.0 %	7.6 %
5.4 %	3.4 %	16.5 %	14.1 %
-1.1 %	-3.0 %	11.4 %	8.3 %
-0.8 %	-2.8 %	12.3 %	8.9 %
-1.6 %	-2.4 %	10.3 %	9.1 %

indicates a stiffening of the structure in the 10 % order from factory values. Comparing experimental data from the first campaign with the second one, there is a frequency shift and a hardening trend. Loss factor retrieved from modal analysis is in the same order of magnitude if compared to literature, confirming the goodness of the measurements [33]. A Normalized Frequency Shift (NFS) is computed as the difference between the corresponding natural frequency in August 2020 and March 2021 of each mode, normalized by the first one. The relation is given in equation (2) as follows:

$$NFS(i) = \frac{f_n^{mar}(i) - f_n^{aug}(i)}{f_n^{aug}(i)} \quad (2)$$

with $i = 1:n$, where n is the number of modes retrieved from modal analysis. Normalized Damping Shift (NDS) is defined in a similar fashion in equation (3) as:

$$NDS(i) = \frac{\eta_n^{mar}(i) - \eta_n^{aug}(i)}{\eta_n^{aug}(i)} \quad (3)$$

As shown in Figure 8, the NFS is almost constant around 14 % [(13.88 ± 0.62) % for wheel 1 and (13.11 ± 0.87) % for wheel 2] of increment and is comparable for both the wheels. As wheel 1 is concerned, data are suggesting a structural stiffening

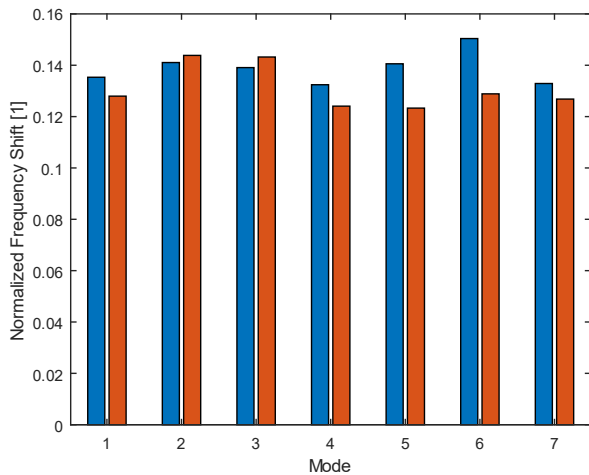


Figure 8. Normalized frequency shift between August 2020 and March 2021 for wheel 1 (blue) and wheel 2 (red).

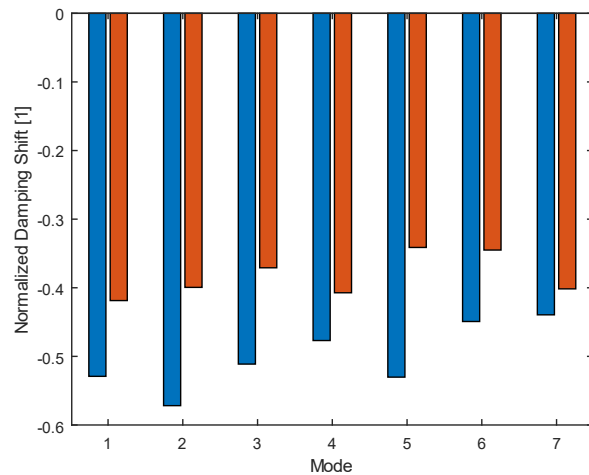


Figure 9. Normalized damping shift between August 2020 and March 2021 for wheel 1 (blue) and wheel 2 (red).

effect. This behaviour is effectively confirmed by literature [27]. Damping undergoes a change as well. This is clearly visible in the NDS indicator shown in Figure 9. In contrast to frequency, there is a decrease of (50.11 ± 4.8) % in the case of wheel 1 and (38.35 ± 3.1) % in the case of wheel 2 due to material ageing. These values suggest a stiffening effect, which is effectively confirmed by the resonance frequency trend variation. This behaviour may be referred to an increase in the glass transition temperature due to environmental ageing of the material, fully curing the samples over time. Increasing the glass transition temperature, the material stiffness increases while its damping capacity decreases at room temperature, causing embrittlement [36]-[39].

4. ENVIRONMENTAL TEST

Material hardening due to ageing has been already investigated in literature for SLA resins [27]. To understand better the reason behind the change over time of the wheel dynamic behaviour, tests varying both temperature and humidity were performed in an environmental chamber. Each test was performed leaving both wheels in the same controlled temperature and humidity conditions for two days. Then, they were weighted and immediately tested, with the same experimental modal analysis setup, to minimize heat transfer with the external environment. For the experiment, only the driving point FRF was obtained as

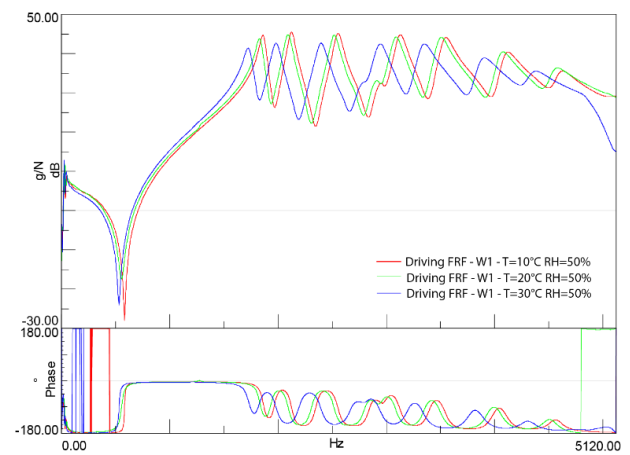


Figure 10. Driving point frequency response function at different temperature and constant humidity.

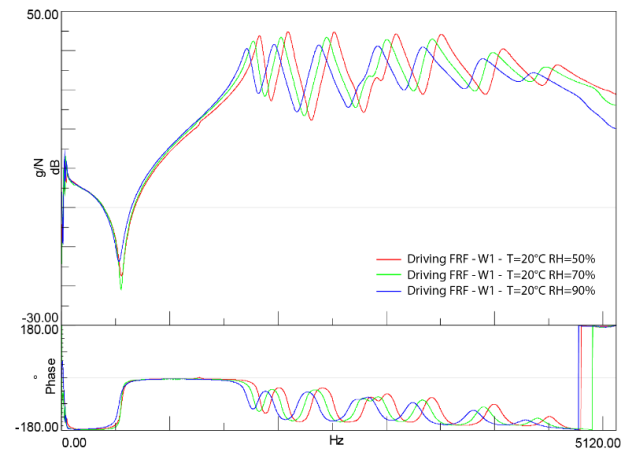


Figure 11. Driving point frequency response function at different humidity and constant temperature.

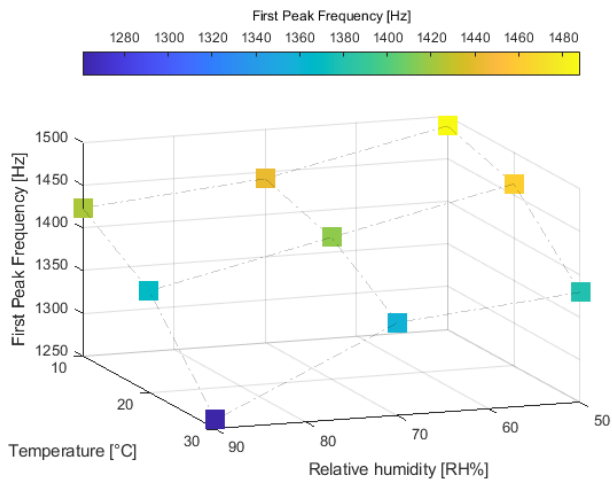


Figure 12. First FRF peak frequency dependence on temperature and humidity for wheel 1.

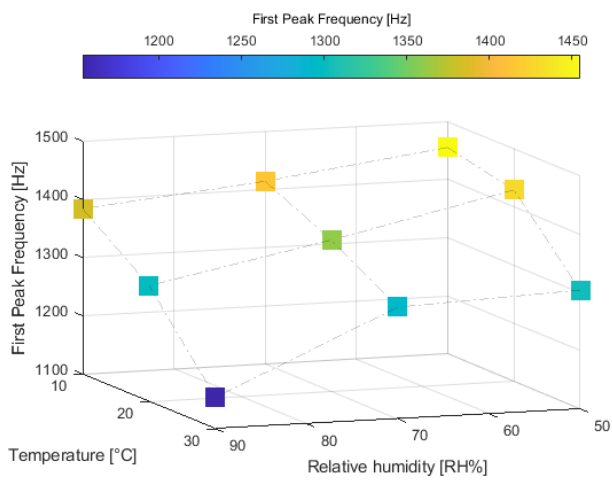


Figure 13. First FRF peak frequency dependence on temperature and humidity for wheel 2.

an average over 3 acquisitions. Tests were performed at temperatures of 10 °C, 20 °C and 30 °C and relative humidity of 50 %, 70 % and 90 %, for a total of nine testing conditions. The driving point FRFs for W1 - different temperatures, same relative humidity - are reported in Figure 10. Increasing temperature, the material undergoes a softening phenomenon, in fact resonances shift towards lower frequencies. Furthermore, also the amplitudes of FRF decrease. Figure 11 shows the driving point FRFs for W1 in the case of constant temperature while relative humidity is varied. Increasing the relative humidity, the material undergoes a softening effect and the FRF amplitudes decrease. To obtain a comprehensive picture of the trend, we chose to consider the first relevant peak of the FRFs for each environmental condition. In Figure 12 and Figure 13, the frequency related to the first resonance peak in the FRF is plotted for each environmental condition for W1 and W2, respectively. The trend surface depicted by the data is clear: increasing both temperature and humidity the material softens. This behaviour is confirmed for both wheels. Putting aside ageing effects on the material and assuming a temperature of 10 °C in March and of 30 °C in August during experiments, at constant humidity of 50 %, the frequency shift relative to temperature variations is nearly 10 %. The shift is in the order of the one found out experimentally and could provide a plausible motivation to the hardening (from warmer to colder – August to March) behaviour

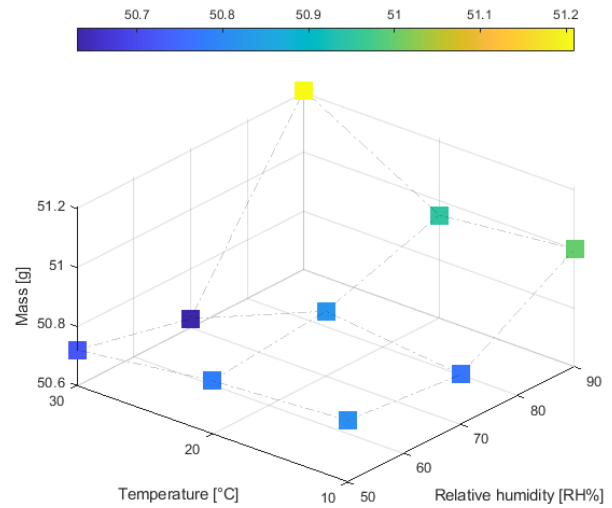


Figure 14. Mass variation dependence on temperature and humidity for wheel 1.

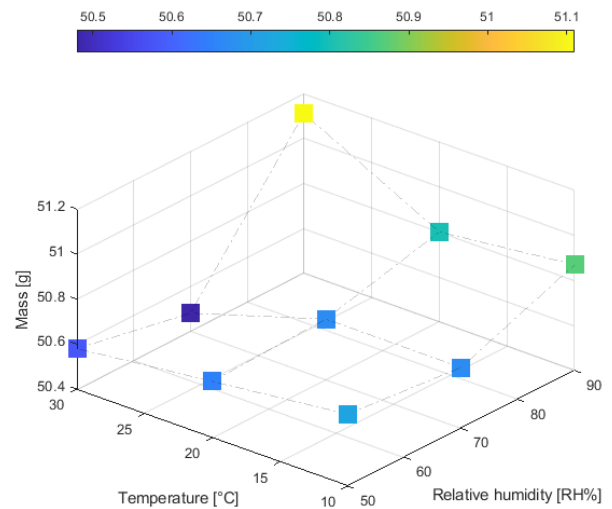


Figure 15. Mass variation dependence on temperature and humidity for wheel 2.

identified. In conclusion, the mass variation with respect to temperature and humidity for both W1 and W2 are shown respectively in Figure 14 and Figure 15. The lowest value is referred to a temperature of 30 °C with 70 % RH whilst the highest to a temperature of 30 °C with 90 % RH for both wheels. The variation between the two environmental conditions is about 0.6 grams for both wheels. To evaluate the weight of this mass variation, an increment in the mass density (equivalent to 1 gram) is introduced in the finite element model described in Section 2. Eigenfrequencies and eigenmodes are computed, leading to a lower frequency shift of 12.5 Hz. A frequency shift of this order is not sufficient to explain the shift present in the experimental data of Figure 12 and Figure 13 for the condition of 30 °C. Therefore, this effect must be due to material softening mostly. The material hardening (from warmer to colder – August to March) behaviour identified could provide a plausible motivation.

5. CONCLUSIONS

The dynamic behaviour of a 3D printed airless wheel is evaluated both by numerical simulation and experimental measurements. The wheel geometry is firstly outlined showing the periodic lattice pattern used. Resonance frequencies with related mode shapes are retrieved from numerical model starting from properties by the manufacturer material datasheet. Experimental modal analysis is performed on wheels in August 2020 and after six months, obtaining modal parameters from the PolyMAX Plus algorithm. Numerical predictions are in line with experimental data, confirming the robustness and the effectiveness of the simulation and its supporting hypotheses. Modal parameters related to both wheels are compared between August 2020 and March 2021. Two normalized parameters are defined to assess the existing frequency and damping shift, obtaining a hardening behaviour characterized by an increase of material stiffness and a decrease in material damping. Moreover, to assess the wheel dynamic behaviour changing over time, tests varying both temperature and humidity were performed in an environmental chamber. An increase in both temperature and humidity lead to material softening, providing a plausible reason for the frequency shift experimentally found.

REFERENCES

- [1] F42 Committee, Terminology for Additive Manufacturing Technologies, ASTM International. DOI: [10.1520/F2792-12A](https://doi.org/10.1520/F2792-12A)
- [2] B. Blakey-Milner, P. Grادل, G. Snedden, M. Brooks, J. Pitot, E. Lopez, M. Leary, F. Berto, A. du Plessis, Metal additive manufacturing in aerospace: A review, *Materials & Design*, vol. 209, p. 110008, 2021. DOI: [10.1016/j.matdes.2021.110008](https://doi.org/10.1016/j.matdes.2021.110008)
- [3] N. Contuzzi, S. L. Campanelli, F. Caiazzo, V. Alfieri, Design and Fabrication of Random Metal Foam Structures for Laser Powder Bed Fusion, *Materials*, vol. 12, 2019. DOI: [10.3390/ma12081301](https://doi.org/10.3390/ma12081301)
- [4] F. Caiazzo, S. L. Campanelli, F. Cardaropoli, N. Contuzzi, V. Sergi, A. D. Ludovico, Manufacturing and characterization of similar to foam steel components processed through selective laser melting, *Int J Adv Manuf Technol*, vol. 92, 2017. DOI: [10.1007/s00170-017-0311-4](https://doi.org/10.1007/s00170-017-0311-4)
- [5] L. J. Kumar, C. G. Krishnadas Nair, Current Trends of Additive Manufacturing in the Aerospace Industry, *Advances in 3D Printing & Additive Manufacturing Technologies*, 2017. DOI: [10.1007/978-981-10-0812-2_4](https://doi.org/10.1007/978-981-10-0812-2_4)
- [6] B.-H. Lu, H.-B. Lan, H.-Z. Liu, Additive manufacturing frontier: 3D printing electronics, *Opto-Electronic Advances*, vol. 1, 2018. DOI: [10.29026/oea.2018.170004](https://doi.org/10.29026/oea.2018.170004)
- [7] Y. Jiang, Md. N. Islam, R. He, X. Huang, P. F. Cao, R. C. Advincula, N. Dahotre, P. Dong, H. F. Wu, W. Choi, Recent Advances in 3D Printed Sensors: Materials, Design, and Manufacturing, *Adv Materials Technologies*, vol. 8, 2023. DOI: [10.1002/admt.202200492](https://doi.org/10.1002/admt.202200492)
- [8] S. Singh, S. Ramakrishna, Biomedical applications of additive manufacturing: Present and future, *Current Opinion in Biomedical Engineering*, vol. 2, 2017. DOI: [10.1016/j.cobme.2017.05.006](https://doi.org/10.1016/j.cobme.2017.05.006)
- [9] M. Touri, F. Kabirian, M. Saadati, S. Ramakrishna, M. Mozafari, Additive Manufacturing of Biomaterials – The Evolution of Rapid Prototyping, *Adv. Eng. Mater.*, vol. 21, 2019. DOI: [10.1002/adem.201800511](https://doi.org/10.1002/adem.201800511)
- [10] P. Lakkala, S. R. Munnangi, S. Bandari, M. Repka, Additive manufacturing technologies with emphasis on stereolithography 3D printing in pharmaceutical and medical applications: A review, *International Journal of Pharmaceutics: X*, vol. 5, 2023. DOI: [10.1016/j.ijpx.2023.100159](https://doi.org/10.1016/j.ijpx.2023.100159)
- [11] A. Farazin, C. Zhang, A. Gheisizadeh, A. Shahbazi, 3D bio-printing for use as bone replacement tissues: A review of biomedical application, *Biomedical Engineering Advances*, vol. 5, 2023. DOI: [10.1016/j.bea.2023.100075](https://doi.org/10.1016/j.bea.2023.100075)
- [12] W. Gao, Y. Zhang, D. Ramanujan, K. Ramani, Y. Chen, C. B. Williams, C. C.L. Wang, Y. C. Shin, S. Zhang, P. D. Zavattieri, The status, challenges, and future of additive manufacturing in engineering, *Computer-Aided Design*, vol. 69, 2015. DOI: [10.1016/j.cad.2015.04.001](https://doi.org/10.1016/j.cad.2015.04.001)
- [13] M. K. Thompson, G. Moroni, T. Vaneker, G. Fadel, R. I. Campbell, I. Gibson, A. Bernard, J. Schulz, P. Graf, B. Ahuja, F. Martina, Design for Additive Manufacturing: Trends, opportunities, considerations, and constraints, *CIRP Annals*, vol. 65, 2016. DOI: [10.1016/j.cirp.2016.05.004](https://doi.org/10.1016/j.cirp.2016.05.004)
- [14] T. D. Ngo, A. Kashani, G. Imbalzano, K. T. Q. Nguyen, D. Hui, Additive manufacturing (3D printing): A review of materials, methods, applications and challenges, *Composites Part B: Engineering*, vol. 143, 2018. DOI: [10.1016/j.compositesb.2018.02.012](https://doi.org/10.1016/j.compositesb.2018.02.012)
- [15] S. A. M. Tofail, E. P. Koumoulos, A. Bandyopadhyay, S. Bose, L. O'Donoghue, C. Charitidis, Additive manufacturing: scientific and technological challenges, market uptake and opportunities, *Materials Today*, vol. 21, 2018. DOI: [10.1016/j.mattod.2017.07.001](https://doi.org/10.1016/j.mattod.2017.07.001)
- [16] A. Morvayová, N. Contuzzi, G. Casalino, Numerical prediction of lack-of-fusion defects in selective laser melted AlSi10Mg alloy, *Materials Science and Technology*, vol. 39, 2023. DOI: [10.1080/02670836.2023.2198889](https://doi.org/10.1080/02670836.2023.2198889)
- [17] A. Morvayová, N. Contuzzi, G. Casalino, Defects and residual stresses finite element prediction of FDM 3D printed wood/PLA biocomposite, *Int J Adv Manuf Technol*, vol. 129, 2023. DOI: [10.1007/s00170-023-12410-0](https://doi.org/10.1007/s00170-023-12410-0)
- [18] Z. Hu, S. Mahadevan, Uncertainty quantification in prediction of material properties during additive manufacturing, *Scripta Materialia*, vol. 135, 2017. DOI: [10.1016/j.scriptamat.2016.10.014](https://doi.org/10.1016/j.scriptamat.2016.10.014)
- [19] Z. Hu, S. Mahadevan, Uncertainty quantification and management in additive manufacturing: current status, needs, and opportunities, *Int J Adv Manuf Technol*, vol. 93, 2017. DOI: [10.1007/s00170-017-0703-5](https://doi.org/10.1007/s00170-017-0703-5)
- [20] A. Morvayova, L. Fabbiano, N. Contuzzi, F. Caiazzo, G. Casalino, On the influence of building position on dimensional accuracy and surface quality of aluminum blocks manufactured by L-PBF, *Optics & Laser Technology*, vol. 167, 2023. DOI: [10.1016/j.optlastec.2023.109830](https://doi.org/10.1016/j.optlastec.2023.109830)
- [21] K. Bertoldi, V. Vitelli, J. Christensen, M. van Hecke, Flexible mechanical metamaterials, *Nat Rev Mater*, vol. 2, 2017. DOI: [10.1038/natrevmats.2017.66](https://doi.org/10.1038/natrevmats.2017.66)
- [22] W. Wu, W. Hu, G. Qian, H. Liao, X. Xu, F. Berto, Mechanical design and multifunctional applications of chiral mechanical metamaterials: A review, *Materials & Design*, vol. 180, 2019. DOI: [10.1016/j.matdes.2019.107950](https://doi.org/10.1016/j.matdes.2019.107950)
- [23] M. Kadic, G. W. Milton, M. van Hecke, M. Wegener, 3D metamaterials, *Nat Rev Phys*, vol. 1, 2019. DOI: [10.1038/s42254-018-0018-y](https://doi.org/10.1038/s42254-018-0018-y)
- [24] S. Wang, M. Zou, Z. Dang, B. Chen, T. Zhou, B. Su, Modelling of flexible metal wheels for planetary rover on deformable terrain, *Thin-Walled Structures*, vol. 141, 2019. DOI: [10.1016/j.tws.2019.01.047](https://doi.org/10.1016/j.tws.2019.01.047)
- [25] C. Suvanjumrat, R. Rugsaj, Study of 3D printing for forming spoke of non-pneumatic tire using finite element method, *IOP Conf. Ser.: Mater. Sci. Eng.*, vol. 1137, 2021. DOI: [10.1088/1757-899X/1137/1/012020](https://doi.org/10.1088/1757-899X/1137/1/012020)
- [26] Y.-S. Zeng, M.-H. Hsueh, T.-C. Hsiao, Effect of ultraviolet post-curing, laser power, and layer thickness on the mechanical properties of acrylate used in stereolithography 3D printing, *Mater. Res. Express*, vol. 10, 2023. DOI: [10.1088/2053-1591/acb751](https://doi.org/10.1088/2053-1591/acb751)

- [27] S. Mansour, M. Gilbert, R. Hague, A study of the impact of short-term ageing on the mechanical properties of a stereolithography resin, *Materials Science and Engineering: A*, vol. 447, 2007. DOI: [10.1016/j.msea.2006.10.007](https://doi.org/10.1016/j.msea.2006.10.007)
- [28] E. Marin, F. Boschetto, M. Zanocco, H. N. Doan, T. P.M. Sunthar, K. Kinashi, D. Iba, W. Zhu, G. Pezzotti, UV-curing and thermal ageing of methacrylated stereo-lithographic resin, *Polymer Degradation and Stability*, vol. 185, 2021. DOI: [10.1016/j.polymdegradstab.2021.109503](https://doi.org/10.1016/j.polymdegradstab.2021.109503)
- [29] C. Tröger, A. T. Bens, G. Bermes, R. Klemmer, J. Lenz, S. Irsen, Ageing of acrylate-based resins for stereolithography: thermal and humidity ageing behaviour studies, *Rapid Prototyping Journal*, vol. 14, 2008. DOI: [10.1108/13552540810907983](https://doi.org/10.1108/13552540810907983)
- [30] K. Altaf, I. A. Ashcroft, N. Saleh, R. Hague, Environmental aging of epoxy based stereolithography parts Part 1 – Moisture transport, *Plastics, Rubber and Composites*, vol. 41, 2012. DOI: [10.1179/1743289811Y.0000000024](https://doi.org/10.1179/1743289811Y.0000000024)
- [31] I. A. Ashcroft, K. Altaf, N. Saleh, R. Hague, Environmental aging of epoxy based stereolithography Part 2 – Effect of absorbed moisture on mechanical properties, *Plastics, Rubber and Composites*, vol. 41, 2012. DOI: [10.1179/1743289811Y.0000000023](https://doi.org/10.1179/1743289811Y.0000000023)
- [32] D. Miedzińska, R. Gieleta, A. Poplawski, Experimental Study on Influence of Curing Time on Strength Behavior of SLA-Printed Samples Loaded with Different Strain Rates, *Materials*, vol. 13, 2020. DOI: [10.3390/ma13245825](https://doi.org/10.3390/ma13245825)
- [33] J. Gietl, J. Vignola, J. Sterling, T. Ryan, Characterization of Damping Properties in 3D Printed Structures, *J. Phys.: Conf. Ser.*, vol. 1149, 2018. DOI: [10.1088/1742-6596/1149/1/012002](https://doi.org/10.1088/1742-6596/1149/1/012002)
- [34] A. Quattrocchi, D. Alizzio, L. Capponi, T. Tocci, R. Marsili, G. Rossi, S. Pasinetti, P. Chiariotti, A. Annessi, P. Castellini, M. Martarelli, F. Freni, A. Di Giacomo, R. Montanini, Measurement of the structural behaviour of a 3D airless wheel prototype by means of optical non-contact techniques, *ACTA IMEKO*, vol. 11, 2022. DOI: [10.21014/acta_imeko.v11i3.1268](https://doi.org/10.21014/acta_imeko.v11i3.1268)
- [35] A. Manesh, M. Tercha, B. Anderson, B. J. Meliska, F. Ceranski, Tension-Based Non-Pneumatic Tire. U.S. Patent 8109308B2, 7 February 2011.
- [36] A. Celli, M. Scandola, Thermal properties and physical ageing of poly (l-lactic acid), *Polymer*, vol. 33, 1992. DOI: [10.1016/0032-3861\(92\)90440-8](https://doi.org/10.1016/0032-3861(92)90440-8)
- [37] P. Lyu, W. Li, Y. Ma, Y. Cui, Effect of ageing on constrained damping structure of viscoelastic material, *AIP Conf. Proc.* 9, 2018. DOI: [10.1063/1.5075656](https://doi.org/10.1063/1.5075656)
- [38] C. Riccio, M. Civera, O. G. Ruiz, P. Pedullà, M. R. Reinoso, G. Tommasi, M. Vollarò, V. Burgio, C. Surace, Effects of Curing on Photosensitive Resins in SLA Additive Manufacturing. *Applied Mechanics* 2, no. 4, 2021. DOI: [10.3390/applmech2040055](https://doi.org/10.3390/applmech2040055)
- [39] M. Štaffová, F. Ondreáš, J. Svatík, M. Zbončák, J. Jančář, P. Lepcio, 3D printing and post-curing optimization of photopolymerized structures: Basic concepts and effective tools for improved thermomechanical properties, *Polymer Testing*, vol. 108, 2022. DOI: [10.1016/j.polymertesting.2022.107499](https://doi.org/10.1016/j.polymertesting.2022.107499)